# Incorporating Priors for Medical Image Segmentation Using a Genetic Algorithm

Payel Ghosh[a, b], Melanie Mitchell[b,c], James A. Tanyi[d] and Arthur Y. Hung[d]

[a]Department of Diagnostic Radiology, UT M.D. Anderson Cancer Center, Houston, TX.
[b]Department of Computer Science, Portland State University, Portland, OR
[c] Santa Fe Institute, Santa Fe, NM.
[d] Department of Radiation Medicine, Oregon Health and Science University, Portland, OR.

*Abstract*— **Medical image segmentation is typically performed manually by a physician to delineate gross tumor volumes for treatment planning and diagnosis. Manual segmentation is performed by medical experts using prior knowledge of organ shapes and locations but is prone to reader subjectivity and inconsistency. Automating the process is challenging due to poor tissue contrast and ill-defined organ/tissue boundaries in medical images. This paper presents a genetic algorithm for combining representations of learned information such as known shapes, regional properties and relative position of objects into a single framework to perform automated three-dimensional segmentation. The algorithm has been tested for prostate segmentation on pelvic computed tomography and magnetic resonance images.**

*Index Terms*—**Medical image segmentation; Genetic Algorithms; Texture Analysis; Shape Modeling; Relative position priors.**

## I. INTRODUCTION

Target-volume and organ-at-risk delineation on medical images such as computed tomography (CT), magnetic resonance imaging (MRI), and ultrasound is quite subjective. The uncertainty and variability in the definition of tumor margins results in suboptimal treatment of patients. The development of automated segmentation tools are therefore essential but remain a challenge for several reasons, such as the variability in organ shapes and tissue contrast on medical images.

Despite advances in imaging for radiation-therapy treatment planning (RTP), most medical image segmentation algorithms require some form of human intervention to perform satisfactorily [2][3][4]. These segmentation algorithms do not incorporate the prior knowledge of human anatomy and representations of known shapes, relative positions of organs, and textures that a human observer uses to manually segment an image. This paper presents a genetic algorithm for combining known priors of shape, texture and relative positions of organs to perform automatic segmentation. Genetic algorithms (GAs) [5] [6] simulate the learning process of biological evolution using selection, crossover and mutation. Genetic algorithms are blind optimization techniques that do not need derivatives to explore the search space; instead they use payoff values known as fitness to guide the search. This quality can make GAs more robust [7] than other local search procedures such as gradient descent or greedy techniques used for combinatorial optimization. GAs have been used for a variety of image processing applications, such as edge detection [8], image segmentation [9], image compression [10], feature extraction from remotely sensed images [11], and medical feature extraction [9]. The image processing problem that has been explored in this paper is image segmentation: a technique for delineating a region of interest on an image.

Level set methods are widely used in the field of medical image segmentation due to their ability to represent boundaries of objects that change with time or are ill-defined [12, 13]. In the level set method, a deformable segmenting curve is associated with an energy function. The energy function may consist of region-based terms (such as pixel intensity values, edges, etc.) and contour-based terms (such as curvature and length of the curve). Here, we have used a genetic algorithm to perform level set curve evolution for performing segmentation. A genetic algorithm (GA) replaces the explicit energy function term used by the level set curve evolution with an implicit fitness function which indirectly correlates texture, relative position and shape information with the evolving curve. This provides a framework for incorporating high-level features and combining multiple priors for segmentation. The level set-based genetic algorithm (LSGA) (introduced by the authors in [1]) uses the learned shape, textural properties of a known object derived from training images to segment thermographic images. This paper presents an extension of the LSGA by incorporating spatial relationships between organs for segmenting images. The individuals of the GA are vectors of parameters of a level set function that the GA optimizes to produce *fit* individuals or good segmentations of a given image. The ability of the LSGA to combine multiple priors for segmentation is the main contribution of this paper. By incorporating derivative-

free optimization for level set function optimization, the LSGA creates a framework for combining multiple features such as shape, texture, relative location information for segmentation. This allows the incorporation of several energy terms into the level set-based contour representation without increasing the computational complexity associated with computing derivatives in conventional curve evolution techniques.

Figure 1 shows a typical pelvic CT scan from a patient suffering from prostate cancer and undergoing radiation therapy. Tumor delineation in the prostate is performed manually by a physician or a medical physicist for identifying treatment locations and determining radiation dosage as shown by the white contour in figure 1. The prostate is located between the bladder and the rectum, which are also labeled in the figure. Since the bladder and the rectum are more texturally prominent on these images; the radiologist uses the locations of these organs to approximately delineate the prostate on these images. Automating this task, therefore, involves incorporating the prior knowledge of shapes, textures and relative positions of organs present in a pelvic scan. The ability of the GA to combine multiple priors for segmentation is the main contribution of this paper. By incorporating derivative-free optimization for level set function optimization, the GA creates a framework for combining multiple features for segmentation. The paper is organized as follows: We first review the current methods and algorithms used for medical image segmentation and discuss the advantage of using a genetic algorithm over conventional optimization methods for level set curve evolution. The methodology is then described followed by the application for prostate segmentation on pelvic CT/MR scans. The strengths and limitations of the GA and future work are discussed at the end.

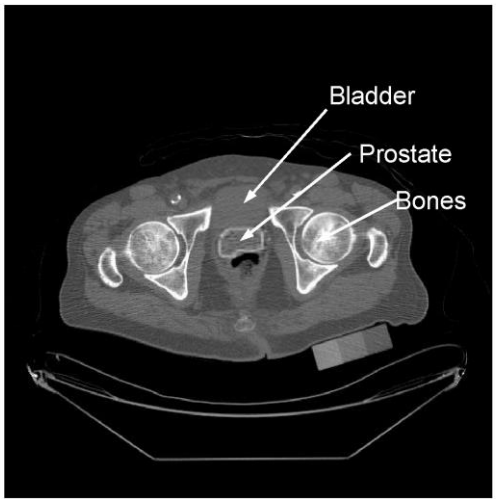


Figure 1 A manually segmented prostate (shown as the white contour) from a single slice of a pelvic CT scan.

## II. LITERATURE REVIEW

Medical images are captured from parts of living organisms so that the structural information contained in them can be quantified and analyzed. They can be acquired in several modalities such as Computed Tomography (CT), Ultrasound (US), Magnetic Resonance Imaging (MRI), Spectroscopy and so on [16]. One of the main challenges of medical image processing is that the information present in these images is usually of a semantic nature. Therefore, an effective mechanism for mapping the pixel-based information to semantic information is needed before this information can be used for accurate diagnosis and treatment planning. Medical image analysis typically involves segmentation, recognition and classification. Here we describe the current state-of-the-art in medical image segmentation and discuss the need to incorporate unconventional optimization techniques such as genetic algorithms for image segmentation.

Segmentation is defined as the process of demarcating an object on an image with a contour. It is performed by determining properties of the object that differentiate it from the rest of the image. These properties can be image pixel-based properties such as edges, texture, pixel intensity variations inside the object, or object-level properties such as shape, size, orientation, location with respect to other objects, etc. The pixel-based features can be extracted using simple image processing routines on an image. For example, edges of an image can be derived using a gradient operator on the image. Texture is a pixel-level feature that quantifies the perceived physical appearance of a surface. Textural segmentation methods can be broadly classified into statistical, spectral and spatial filtering methods, and model-based methods. Statistical approaches such as moment-based methods [17], co-occurrence matrices [18] etc., quantify textures like coarse, grainy, smooth, etc. Spectral and spatial filtering methods try to simulate the human visual system [19] by performing local spectral frequency analysis [20][21][22][23]. Model-based methods such as Markov random fields (MRF) [24][25] and fractal-based modeling [26] have also been used for texture segmentation. One major drawback of all pixel-based segmentation algorithms is that there is no notion of shape in these methods and they can identify regions outside the object as being part of the object and. We demonstrate the outcome of using a texture-only approach on the problem of prostate segmentation using Gabor wavelets, described in the following section. Pixel-based operations are more suitable for problems where objects have prominent edges and markedly different textures inside and outside the object. Most medical images have noise and artifacts that appear during the image acquisition process and suffer from low contrast with broken/diffuse edges around regions of interest. Therefore, often an object-based approach or a combination of pixel and object-based techniques are more suitable for medical image segmentation.

Active-contour models are shape-based procedures where an energy function minimization drives contour deformation [27, 28, 29]. Leventon et al. [31] introduced statistical shape priors into their geodesic active-contour model to generate maximum *a posteriori* estimates of pose and shape. They segmented synthetic as well as medical images using their method and compared level-set evolution with and without shape influence. Tsai et al. [32] derived a shape-based level set function using statistics defined over local regions in a set of training images. They showed automatic segmentation results on several synthetic images and semi-automatic segmentation on cardiac and pelvic MRI images. Shape priors have also been used with active-contour-based image segmentation by Etyngier et al. [33]. They used diffusion maps to model shapes as finite-dimensional manifolds. Their segmentation results were accurate but the initial contour was placed manually in the images. Chan and Vese introduced a region-based energy function based on the piece-wise constant Mumford-Shah model [34], in order to detect features with diffuse boundaries. Their energy functional for curve evolution is given by:

$$F(c_1, c_2, C) = \mu \cdot length(C) + \upsilon \cdot Area(inside(C)) + \lambda_1 \int_{inside(C)} \left| u_0(x,y) - c_1 \right|^2 dxdy + \lambda_2 \int_{outside(C)} \left| u_0(x,y) - c_2 \right|^2 dxdy. \quad (1)$$

Here $C$ is the evolving contour, $u_0$ is the pixel intensity value, $c_1$ and $c_2$ are averages of pixel intensity values inside and outside the segmenting contour and $\mu \geq 0, \upsilon \geq 0, \lambda_1, \lambda_2 > 0$ are fixed parameters. We show sample pelvic segmentation using the Chan and Vese algorithm to compare an active contour methodology with our segmentation approach.

Much current research work on image processing is focused on spatial knowledge representation for applications such as medical imaging [35], geographical information systems (GIS) [36], robot tracking [37] etc. Spatial relationship features are described by the relative position of an object in an image with respect to a reference object. Common methods for deriving spatial relationships include topological methods, distance and direction-based methods [38]. Spatial relationships have the ability to describe scenes [39] on images using concepts such as near/far, inclusion/overlap, above/below, etc. Some recent methods for quantifying spatial relations on images are Bayesian network classifiers [40] [41], graph matching methods [42], and fuzzy relative location maps [43]. The fuzzy relative location method described in [43, 44] has been incorporated into the GA because it can be used to locate objects in images with poor contrast and ill-defined boundaries such as the prostate on pelvic CT/MRI images.

### *A. Genetic Algorithms*

Evolutionary computation methods such as genetic algorithms are useful for medical image analysis because they can model the inherent uncertainties of medical images caused by poor contrast, ill-defined boundaries and subjectivity. Genetic algorithms simulate the process of biological evolution using the principle of survival of the fittest. GAs have been used for a variety of optimization problems, such as image enhancement [45], feature extraction from remotely sensed images [46], and image segmentation [47]. In contrast with traditional optimization methods, a GA uses a stochastic parallel search to reach the optimum solution and so is less likely to become stuck in a local maximum. At each generation a new population is generated and the fitness values of all individuals are evaluated based on their performance in the problem domain. The process of selection, crossover, and mutation is repeated until offsprings with acceptable fitness values are produced.

A GA stochastically searches the space of candidate solutions to identify the globally optimal solution for a given problem. Individuals of the GA are candidate solutions and are typically encoded as bit strings or vectors [48] (also known as chromosomes) whose interpretation depends on the application. The chromosome is the genetic makeup of an individual and is also known as the *genotype*. The genotypes are uniquely mapped to the solution domain (known as the *phenotype*). The fitness function is used to measure the performance of each individual in the problem domain. In multi-objective optimization problems more than one objective functions or fitness functions are simultaneously optimized during the evolutionary search process. Fitness functions are usually specified by the user depending on the application. In this paper, we have adopted the fitness function from [9] as described in the following section. Selection is the process of choosing an individual for propagating their genes (bit strings) to future generations. It is performed in a number of different ways such as rank selection, fitness proportionate selection, and tournament selection. Crossover and mutation operators are then applied to produce new offsprings that are members of the next generation. Single-point crossover swaps same length segments of genes between two parents to produce the offspring. The mutation operator randomly modifies the value of a gene. The GA is usually terminated if the fitness value attained in a generation exceeds a certain threshold or a certain pre-specified number of generations have been produced.

Genetic algorithms have been used for segmentation by other groups [47, 49, 50, 51, 52]. In [52] a genetic algorithm template matching (GATM) scheme was introduced to automatically detect lung nodules in thoracic CT images. Phantom images of the lung nodule phantom and global nodule intensity distribution were used for template matching. The paper

suggests that genetic-algorithm-based methods are very useful for medical imaging applications. Another recent work using GAs for medical image segmentation was by Chabrier et al. [53]. They used a GA to find the optimal combination of information extracted from several different segmentation algorithms. The GA described in this paper evolves parameters of a level set function. Cagnoni et al. [51] used a GA for interactive image segmenting by evolving parameters of an active contour model called snakes [54]. The GA optimized an energy function based on features such as smoothness of the curve, curvature and image gradient. Unlike the explicit representation of shapes used by [51], our method uses the level set-based implicit representation of shape, which allows the inclusion of textural and spatial relationship features for searching the parameter space. A model-based image analysis technique using a GA is described in [55]. The method uses an evolutionary Hough transform scheme to detect objects with known shapes on images such as circle and ellipse. Here, the GA population consists of a set of points in the parameter space. In contrast, the LSGA evolves a population of segmenting contours constrained by known shape.

## III. Method

The GA presented here consists of two phases: the training phase and the segmentation phase. In the training phase, shape, shape variability, texture, and relative position information of the organs of interest are derived from images manually segmented by a human observer. The training contours provide information about the shape and position of the given object. The textural properties of the object are derived from the training data using image processing routines. In the segmentation phase the genetic algorithm evaluates candidate segmenting contours for delineating the desired object on a new image using a fitness measure, and iterates until a stopping criterion is satisfied.

### *A. Shape model*

The shape representation is derived from the mean and variance of all manually drawn contours in the training set. Before deriving the mean shapes and shape variances from the training data, the images are aligned for pose. The manually drawn contours from the training data are first converted into signed distance functions $\psi_i$ ($i$ = 1 to $n$, where $n$ is the number of training contours). Converting the contours to signed distance representations makes it easy to derive the mean shape and shape variability using matrix transformations without finding point correspondences. Following [32], the level set function is defined as a linear combination of the mean shape and weighted shape variances in the signed distance domain. The mean shape is defined for $n$ contours as:

$$\bar{\boldsymbol{\Phi}} = (\frac{1}{n})\sum_{i=1}^{n} \boldsymbol{\psi}_i. \tag{2}$$

Mean offset functions are derived by subtracting the mean contour from each training contour in the signed distance domain ( $\tilde{\boldsymbol{\psi}}_i = \boldsymbol{\psi}_i - \bar{\boldsymbol{\Phi}}$ ). The columns of the mean offset functions (size $N = N_1$ x $N_2$, the same as the training images) are then successively stacked on top of one another to form one large column vector ( $\mathbf{S}_i$ ) of size 1 x $N$. A new matrix $\mathbf{S}$ (size $N$ x $n$), called the shape variability matrix, is formed from $n$ such column vectors,

$$\mathbf{S} = [\mathbf{S}_1, \mathbf{S}_2, ..., \mathbf{S}_n]. \tag{3}$$

The variance in shape is then computed by an Eigen-value decomposition on this shape variability matrix as,

$$\frac{1}{n}\mathbf{S}\mathbf{S}^T = \mathbf{U}\boldsymbol{\Sigma}\mathbf{U}^T. \tag{4}$$

Here $\mathbf{U}$ is an $N$ x $n$ matrix whose columns represent $n$ orthogonal modes of shape variation and $\boldsymbol{\Sigma}$ is a diagonal matrix of Eigen values. By rearranging the columns of $\mathbf{U}$ to form an $N_1$ x $N_2$ structure, the $n$ different Eigen shapes $\{\boldsymbol{\Phi}_1, \boldsymbol{\Phi}_2, ..., \boldsymbol{\Phi}_n\}$ can be obtained. The mean shape and shape variability are then used to define a level set function [32],

$$\boldsymbol{\Phi}[\mathbf{w}] = \bar{\boldsymbol{\Phi}} + \sum_{j=1}^{k} w_j \boldsymbol{\Phi}_j. \tag{5}$$

Here $\boldsymbol{w}$ are the weights for linearly combining the $k$ principal Eigen shapes. By incorporating pose parameters into this level set framework, a new level set function is obtained, that can handle object shapes with different sizes and orientation. Pose is defined using an affine transform $\mathbf{T}[\boldsymbol{p}]$, which is the product of three matrices, the translation matrix, the scaling matrix and the rotation matrix respectively,

$$\begin{bmatrix} \tilde{x} \\ \tilde{y} \\ 1 \end{bmatrix} = \begin{bmatrix} 1 & 0 & a \\ 0 & 1 & b \\ 0 & 0 & 1 \end{bmatrix} \begin{bmatrix} h & 0 & 0 \\ 0 & h & 0 \\ 0 & 0 & 1 \end{bmatrix} \begin{bmatrix} \cos\theta & -\sin\theta & 0 \\ \sin\theta & \cos\theta & 0 \\ 0 & 0 & 1 \end{bmatrix} \begin{bmatrix} x \\ y \\ 1 \end{bmatrix}. \tag{6}$$

Here, $\boldsymbol{p} = [a, b, h, \theta]$, $a$, $b$ are $x$, $y$ translation parameters, $h$ is the scale factor and $\theta$ is the angle of rotation. The pixel coordinates of the input image $(x, y)$ are mapped to $(\tilde{x}, \tilde{y})$ of the affine transformed image. The new level set function incorporating pose parameters is defined as [32]:

$$\boldsymbol{\Phi}[\mathbf{w}, \mathbf{p}](x, y) = \bar{\boldsymbol{\Phi}}(\tilde{x}, \tilde{y}) + \sum_{j=1}^{k} w_j \boldsymbol{\Phi}_j(\tilde{x}, \tilde{y}). \tag{7}$$

The zero level of this level set function gives the segmenting contour. The genetic algorithm presented in this paper optimizes the $\boldsymbol{w}$ (the weights for combining the Eigen shapes) and $\boldsymbol{p}$ (pose) parameters of this level set function using combinations of pixel-based textural features and spatial relationships for segmentation.

### *B. Textural feature extraction*

The textural feature priors are derived from training images using the Gabor wavelet transform method. Gabor wavelets are unique because they achieve the maximum joint space-frequency resolution thereby characterizing both coarse and fine features. This property makes them a good choice for textural feature segmentation where textural features need to be localized both in space and frequency.

Gabor wavelets are based on the Gabor elementary function given by the modulation of the Gaussian with a complex exponential function as shown in equation (8).

$$h(x,y) = g(x,y)\exp\left[j2\pi Wx\right],\ g(x,y) = \frac{1}{2\pi\sigma_x\sigma_y}\exp\left\{-\frac{1}{2}\left[\left(\frac{x}{\sigma_x}\right)^2 + \left(\frac{y}{\sigma_y}\right)^2\right]\right\}. \tag{8}$$

Here $W$ is the modulation frequency, and $\sigma_x$, $\sigma_y$ characterize the bandwidth of the filter. Gabor wavelets are derived by several translations and dilations of the mother wavelet $h(x, y)$. The method of Gabor wavelets assumes that local texture regions are spatially homogeneous. The mean and standard deviation of the transform coefficients are used to represent regions for classification. The Gabor wavelets are obtained from the generating function,

$$\begin{gathered} h_{mn}(x,y) = a^{-m}H(x',y'), \mathrm{a} > 1, \\ \text{and } x' = a^{-m}\left(xCos\frac{n\pi}{k} + ySin\frac{n\pi}{k}\right), y' = a^{-m}\left(-xSin\frac{n\pi}{k} + yCos\frac{n\pi}{k}\right). \end{gathered} \tag{9}$$

Here, $k$ is the number of orientations, $H$ is the Fourier transform of $h(x, y)$, and $m$ and $n$ specify the scale and orientation of the wavelet. Here we have used $m \in \{0,1,2,..,99\}$ and $n \in \{0,1,2\}$. Given an image $\boldsymbol{I}(x, y)$, the Gabor wavelet transform is given by equation (10) where, $h^*$ is the complex conjugate of $h$

$$W_{mn}(x,y) = \int I(x_1,y_1)h^*_{mn}(x-x_1, y-y_1)dx_1dy_1. \tag{10}$$

The textural segmentation on the test image along with the spatial relationship map is used to determine the fitness of an individual segmenting contour.

### *C. Deriving spatial relationships*

The fuzzy landscape approach introduced by [43] has been incorporated into the GA to represent spatial relations between objects on an image. In this method, fuzzy distance and direction maps are created from a reference object to the target object. On fuzzy maps, regions with higher gray-level values are regions with higher fuzzy membership values depicting a greater likelihood of finding the target object with respect to the reference object.

Fuzzy distance relations such as *near* and *far* are defined using a fuzzy interval *f* of trapezoidal shape on the space of distances (shown in Figure 2). For the *near* relation, the limits of the fuzzy interval ($n_3$, $n_4$) are determined using the largest distance between points in reference object and target object. Similarly, for the *far from* relation, the prior knowledge of the nearest distance between the two objects is used to derive the limits of $f(n_1, n_2)$ such that $0 \le n_1 \le n_2 \le n_3 \le n_4$. The fuzzy subset of the image space is obtained by applying $f$ to the distance map $d_A$ of the reference object $A$:

$$\mu_d(P) = f(d_A(P)), \tag{11}$$

where $P$ is any point in the image.

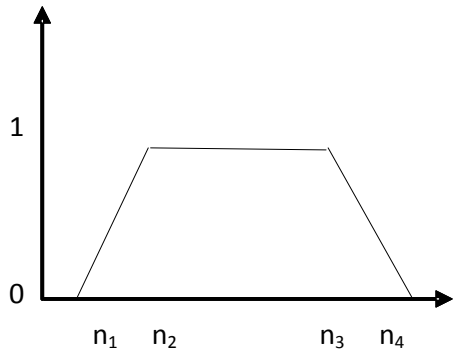


Figure 2. Fuzzy interval *f* used to define relations such as *far* and *near*.

To derive the angle maps, a vector joining the point $P$ in the image space to the point $Q$ in the reference object is created. Then the angle between the vectors **QP** and **u**, and the unit vector in the direction under consideration $\beta(P,Q)$, is computed in the range $[0,\pi]$. Here $Q$ has been taken as the centroid of the reference object. The fuzzy subset of the image space is then defined as

$$\mu_\alpha(P) = g(\beta(P,Q)),\ g(\theta) = \max[0, 1-(2/\pi)\theta]. \tag{12}$$

Here, $g$ is a decreasing function which maps the range of angles $[0, \pi]$ to [0, 1]. Figure 3 shows fuzzy distance and angle maps from the reference object on top to the target object on bottom. For all training contours, the fuzzy interval limits $n_1$, $n_2$, $n_3$, $n_4$ are first derived. The final fuzzy distance map ( $\mu_d$ ) is derived from all the training images by setting the fuzzy interval limits to minimum ($n_3$), maximum ($n_4$), minimum ($n_1$), maximum ($n_2$). The fuzzy direction map is created by finding the mean direction between the reference object and the target object and applying a decreasing function $g$ to it ( $\mu_\alpha$ ).The intersection of the fuzzy distance and direction map is then computed to derive the fuzzy landscape ( $\mu$ ) from the reference object to the target object.

$$\mu_i = \mu_d \cdot \mu_\alpha, \text{ where, } i = 1, ...., o. \tag{13}$$

Here $o$ refers to the total number of reference objects. For multiple reference objects and one target object (for example reference objects: bladder and rectum; and target object: prostate) the union of the fuzzy landscapes from each reference object is derived to compute the final fuzzy landscape (equation 14 and figure 4).

$$\mu = \mu_1 + \mu_2 + ... + \mu_o. \tag{14}$$

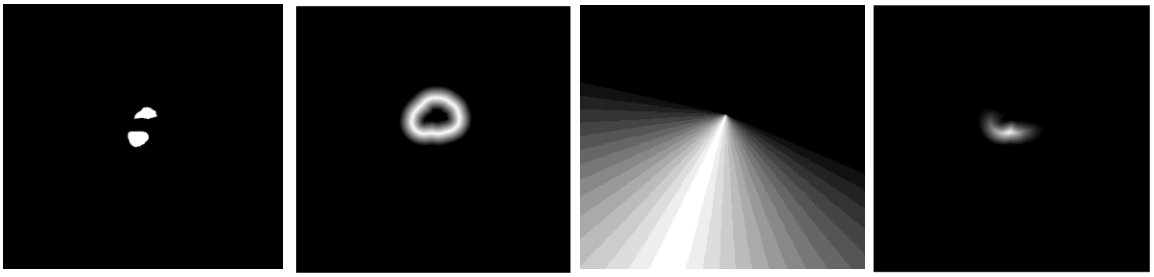

Figure 3. Left-most panel: Reference object (top), target object (bottom); Second panel: The fuzzy distance map; Third panel: The fuzzy angle map; Right-most panel: The fuzzy landscape intersection of the fuzzy distance and angle maps.

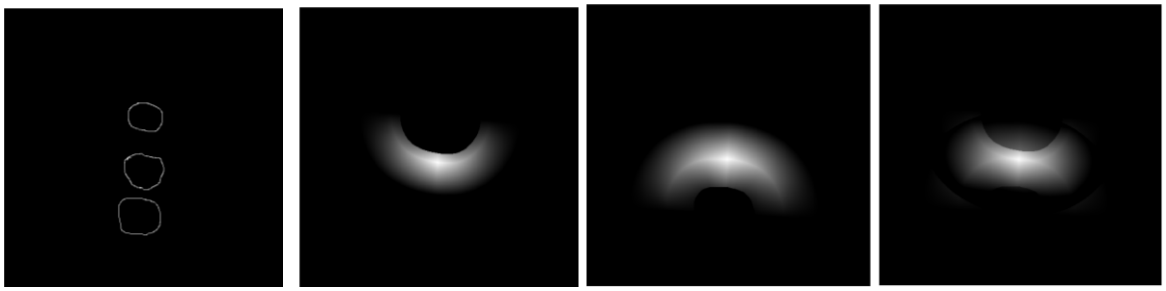

Figure 4. Left panel: Reference objects $R_1$ (above) and $R_2$ (below) and target object ($T_1$) in the center. Second panel: Fuzzy landscape ( $\mu_1$ ) derived from $R_1$-$T_1$. Third panel: Fuzzy landscape ( $\mu_2$ ) derived from $R_2$-$T_1$. Right panel: Final fuzzy landscape ( $\mu$ ) created by the union of $\mu_1$ and $\mu_2$ .

### *D. Segmentation Stage*

Segmentation is performed by identifying the optimal contour enclosing the object with the desired shape, texture, relative position from its neighbors. Each individual in the 2D GA population is defined as a fixed-length *chromosome* of real-valued *genes* as:

$$Individual = [w_1, w_2, w_3, w_4, a, b, h, \theta]. \quad (15)$$

The four weight parameters are used for deriving the weighted $\pm\sigma_1$ and $\pm\sigma_2$ variation (where $\sigma_i^2$ is the Eigen values corresponding to $i$ principal Eigen shapes) of the mean shape and $a$, $b$, $h$, and $\theta$ are pose parameters as defined in equation 6. The pose parameters are chosen randomly from the space of real numbers. Each individual in the population represents a unique segmenting contour. The fitness of an individual is calculated based on the degree to which the segmenting contour encloses the region of interest (ROI) on a test image (a new image not in the training set).

The region of interest is given by the gray-scale image **P** which is the dot product of the binary texture segmentation on the test image (**B**) and the fuzzy relative position map derived from training images (**RL**). Therefore, each pixel in the texture segmentation is weighted by the fuzzy membership value of its location relative to the prostate.

$$P = B \bullet RL \quad (16)$$

The binary image ($\mathbf{B}_1$) is obtained by placing the segmenting contour on the test image and classifying all pixels inside the contour as *true* and all other pixels as *false*. A higher fitness score suggests that more pixels inside (outside) the contour belong to the desired (other) texture type and also satisfy the spatial relationships that were derived from the training data. The fitness is a function of the detection rate ($D$) and the false alarm rate ($F$):

$$\text{Fitness} = 500(D + (1 - F)), \quad (17)$$

The detection rate is defined as the mean value of pixels in **P** inside the segmenting contour $\mathbf{B}_1$. The false alarm rate denotes the mean value of pixels in **P** that lie outside the segmenting contour of $\mathbf{B}_1$. The detection rate and false alarm rate is determined from the mean of the pixel values in **P** that match the segmented contour in $\mathbf{B}_1$. The multiplication factor of 500 rescales the range of fitness values from [0, 2] to [0, 1000] so that we can report fitness values up to three significant digits. The processes of GA evolution: selection, crossover, and mutation are iterated to create successive generations until an individual with high fitness value is created or after a specified number of generations have been produced.

## *E. Extension to three dimensions (3D)*

The extension of the GA to three-dimensions uses 3D pose parameters; *x*, *y*, *z* translation (*a*, *b*, *c*), scale (*h*), yaw ($\alpha$), pitch ($\beta$) and roll ($\theta$).

$$\begin{bmatrix} \tilde{x} \\ \tilde{y} \\ \tilde{z} \\ 1 \end{bmatrix} = \begin{bmatrix} 1 & 0 & 0 & a \\ 0 & 1 & 0 & b \\ 0 & 0 & 1 & c \\ 0 & 0 & 0 & 1 \end{bmatrix} * \begin{bmatrix} h & 0 & 0 & 0 \\ 0 & h & 0 & 0 \\ 0 & 0 & h & 0 \\ 0 & 0 & 0 & 1 \end{bmatrix} * \mathbf{R}_x * \mathbf{R}_y * \mathbf{R}_z * \begin{bmatrix} x \\ y \\ z \\ 1 \end{bmatrix}. \tag{18}$$

$\mathbf{R}_x$, $\mathbf{R}_y$, and $\mathbf{R}_z$ are the rotation matrices about the *x*, *y* and *z* axes respectively:

$$\mathbf{R}_x = \begin{bmatrix} 1 & 0 & 0 & 0 \\ 0 & \cos(\alpha) & -\sin(\alpha) & 0 \\ 0 & \sin(\alpha) & \cos(\alpha) & 0 \\ 0 & 0 & 0 & 1 \end{bmatrix}, \mathbf{R}_y = \begin{bmatrix} \cos(\beta) & 0 & \sin(\beta) & 0 \\ 0 & 1 & 0 & 0 \\ -\sin(\beta) & 0 & \cos(\beta) & 0 \\ 0 & 0 & 0 & 1 \end{bmatrix}, \mathbf{R}_z = \begin{bmatrix} \cos(\theta) & -\sin(\theta) & 0 & 0 \\ \sin(\theta) & \cos(\theta) & 0 & 0 \\ 0 & 0 & 1 & 0 \\ 0 & 0 & 0 & 1 \end{bmatrix}. \tag{19}$$

The 3D GA individual is defined as:

$$Individual = [w_1, w_2, a, b, c, h, \alpha, \beta, \theta]. \tag{20}$$

The mean shape and shape variability are computed by stacking all the slices of the CT/MR scans from the training data as shown in figure 5. The 3D segmenting surface generated by the GA segments all the slices of a test image simultaneously.

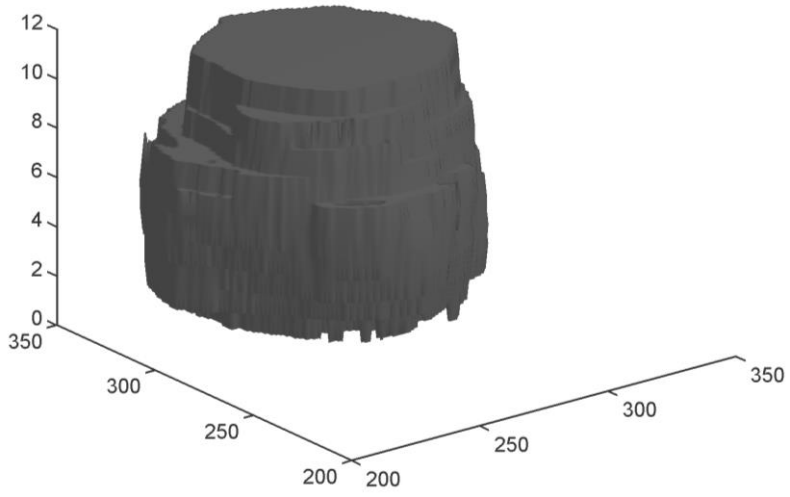


Figure 5. A sample 3D-GA individual [4554, 1595, 5, 12, 1, 1.4, 0, 0, 0].

## IV. PROSTATE SEGMENTATION

The prostate gland is a male reproductive organ located below the bladder and in front of the rectum and is about 3 cm in length along the height of the body. The almond-shaped prostate gland can be deformed by bladder and rectal filling and its size can vary considerably across patients making automatic segmentation a challenging problem.

The pelvic images were obtained from CT and MRI scans of patients being treated for Prostate Cancer at Oregon Health & Science University (OHSU). CT and MRI images of 10 patients (for each modality) were manually segmented by Dr. A. H. and Dr. J. T, (Dept. of Radiation Medicine, OHSU). The CT and MRI images were acquired using 16-slice big-bore configuration Computed Tomography simulator (Brilliance 190P; Philips Medical Systems, Cleveland, OH, USA) and 3-Tesla whole-body Magnetic Resonance Imaging instrument (Trio; Phillips Medical systems, Malvern, PA, USA) respectively.

Each scan for a patient contained ~15 two-dimensional (2D) slices. The prostate was visible in about 10-12 of these slices; the rest displayed other organs in the pelvic region such as the bladder and the rectum. The prostate, bladder and rectum were manually segmented on each scan. The manually segmented contours derived from the scans of five patients (~50x2=100 images) were used as the training data for this analysis. The images from the other five patients were used as test images. Note that the CT and MRI images for this analysis were derived from different patients.

## V. EXPERIMENTS

As a pre-processing step, the CT images were brightened to improve the visibility of soft-tissue regions using the *imadjust* function in MATLAB™. They were also filtered using an averaging filter to remove streak artifacts. The MRI images already had good contrast, so contrast-enhancement was not performed on them. However some of the images were filtered using an averaging filter to smooth speckle noise. The GA was then implemented using texture, shape, and relative location priors for segmenting 2D and 3D CT and MRI images.

### *A. Segmentation in two dimensions (2D)*

At first the mean shape and shape variability of the prostate was derived from the training images as shown in figure 6. The fuzzy relative location was derived from the training images using the method described in the previous section.

Here, the bladder and rectum were used as reference objects and the prostate was the target object. The fuzzy landscape was derived from all training images using both bladder and the rectum as the reference objects as shown in figure 7.

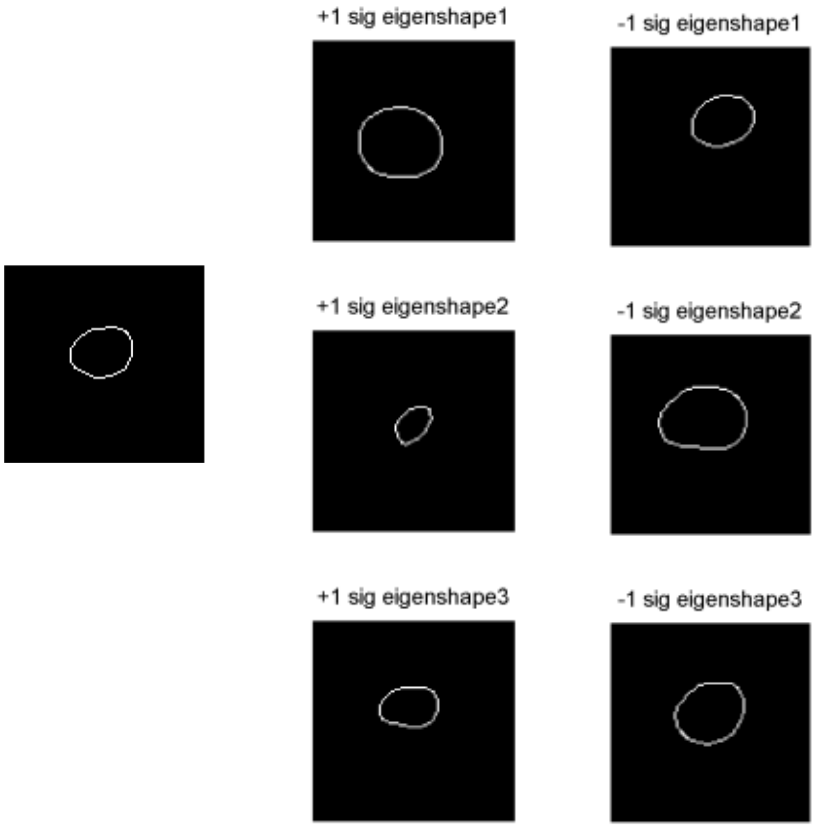


Figure 6. Mean shape (left panel) and shape variability (right panel) of the prostate derived from training images.

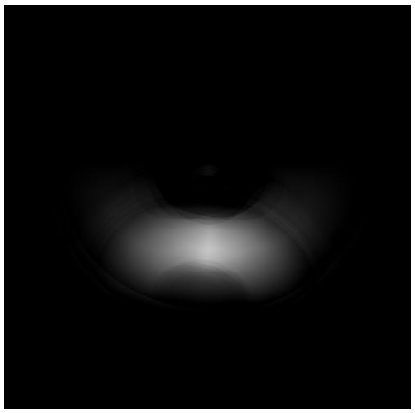

Figure 7 The fuzzy landscape derived from all training images using the bladder and rectum as the reference objects.

On test images, multi-class texture segmentation was performed for the following classes: prostate, bladder, rectum and background as shown in figure 8. This step was incorporated to narrow down the textural search space for the GA. The GA used the textural information and the fuzzy landscape information to derive the final segmenting contour on the test image.

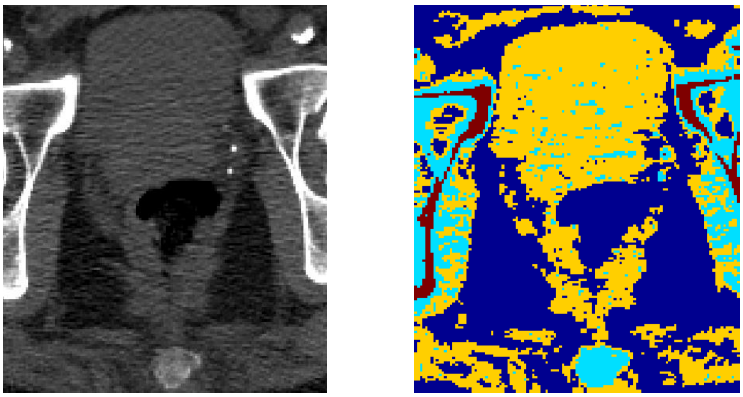

Figure 8. Multiclass texture segmentation of a pelvic CT image using the Gabor wavelet transform.

The initial population of the GA was generated using values chosen randomly from the range of parameter values specified in Table 1. The parameter values were substituted into the level set equation 7, to generate segmenting contours constrained by the known shape of the prostate. The fitness of each individual was computed by comparing the degree of overlap between the segmenting contour and the region of interest on a test image. Here, textural priors generated by Gabor wavelet transform method and the relative position priors were used to narrow the region of interest. The GA was iterated by performing selection, cross-over and mutation over 30 generations or until the threshold exceeded the threshold value of 900 (user specified out of maximum value of 1000) to obtain the final segmenting curve.

Table 1. GA parameters for 2D segmentation

| | |
|---|---|
| Population Size | 50 |
| Mutation Rate | 10 % per gene |
| Crossover Rate | 50% single-point |
| Selection Criteria | Rank Selection |
| Weights for eigen shapes, $w$ | (0- ± 2)integers * $\sigma_i$ |
| Translation parameters $a$, $b$ | Integer (0-30) |
| Rotation parameter $\theta$ | -30° to +30° |
| Scale parameter $h$ | (0.5-2) |

## *B. Segmentation in 3D*

Three-dimensional segmentation was performed by simultaneously segmenting all the slices of a test image at once using a segmentation surface (using parameters specified in Table 2). The mean shape and shape variability were derived in 3D as shown in Figure 9. The segmenting surface simultaneously placed a segmenting contour on all slices of the CT/MRI scans from a patient. Textural features and the fuzzy spatial landscape were derived in 2D as described previously. The fitness of the segmenting contour was computed by averaging over all 2D segmenting contours represented by the 3D GA individual. The GA performed selection, crossover and mutation to derive the final 3D segmenting surface that segmented all the slices of a test image at once.

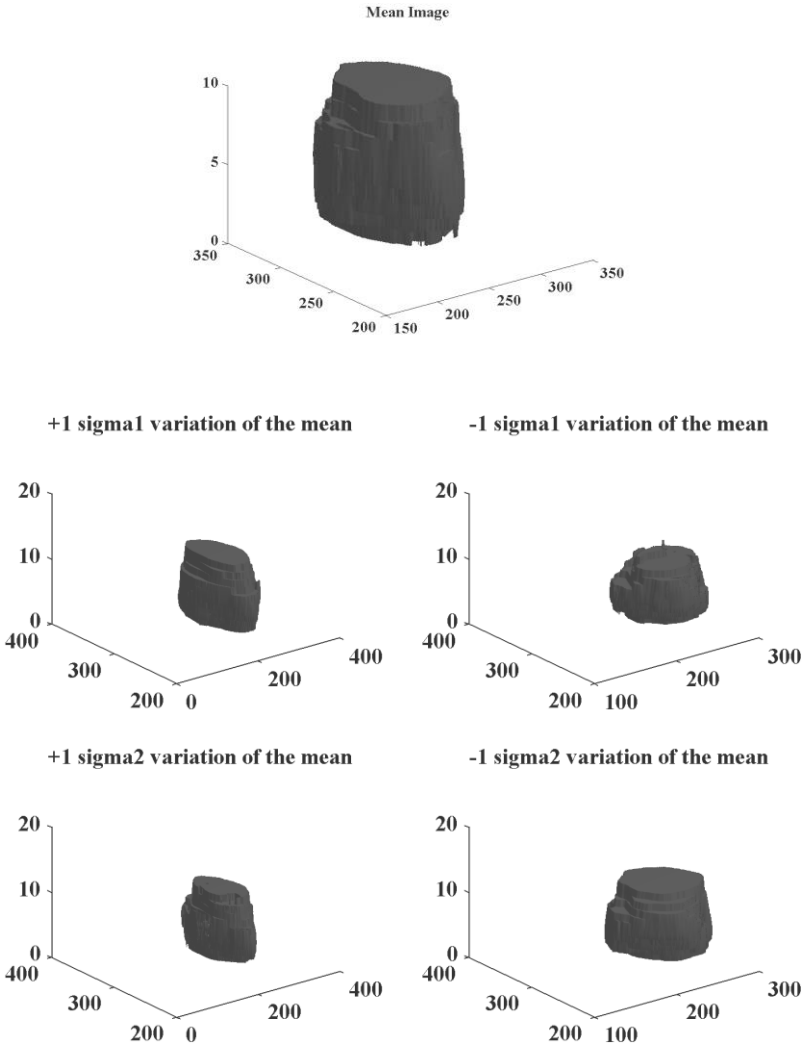


Figure 9. Mean shape (top) and shape variability (bottom) of the prostate derived from training images.

Table 2 GA parameters for 3D segmentation

| | |
|---|---|
| Population Size | 25 |
| Mutation Rate | 10 % per gene |
| Crossover Rate | 50% single-point |
| Selection Criteria | Rank Selection |
| Weights for eigen shapes, $w$ | (0 - ± 2) integers * $\sigma_i$ |
| Translation parameters $a$, $b$, $c$ | Integer (0-20) |
| Rotation parameters $\alpha$, $\beta$, $\theta$ | -30° to +30° |
| Scale parameter $h$ | (0.5-2) |

### C. *Evaluation Criteria*

For evaluating the performance of the algorithm the definitions of closeness of the segmentation outcome to the truth (here, manual segmentation) were derived using the dice similarity coefficient [56]. The dice similarity coefficient provides a measure of the degree of overlap between two segmentations as:

$$DSC(\mathbf{A},\mathbf{B}) = \frac{2\left|\mathbf{A} \cap \mathbf{B}\right|}{\left(\left|\mathbf{A}\right| + \left|\mathbf{B}\right|\right)}, \tag{21}$$

where, **A** is the segmenting contour and **B** is the ground truth derived from manual segmentation. A *DSC* of 1 indicates a perfect match and 0 indicates no match. The ground truth was obtained by averaging over multiple manual delineations.

## VI. Results And discussion

To compare our approach with an active contour method, the Chan and Vese algorithm was used to segment a test images. The initial contour was placed in the center of each test image (left panel of Figure 10). The right panel of Figure 10 shows the outcome of the algorithm for a CT image. The algorithm found boundaries between the regions with markedly different pixel intensity values. The obtained result was expected because the algorithm is designed to find regions with different pixel intensity values inside and outside the contour and it does not constrain the evolving contour using a known shape prior. Similarly, the textural segmentation outcome of Gabor Wavelet transform (Figure 8), shows that pixels outside the prostate region (in the bladder and soft tissue regions surrounding the prostate) were labelled belonging to the same class as the prostate, because the method by itself can only discriminate regions of high contrast differences.

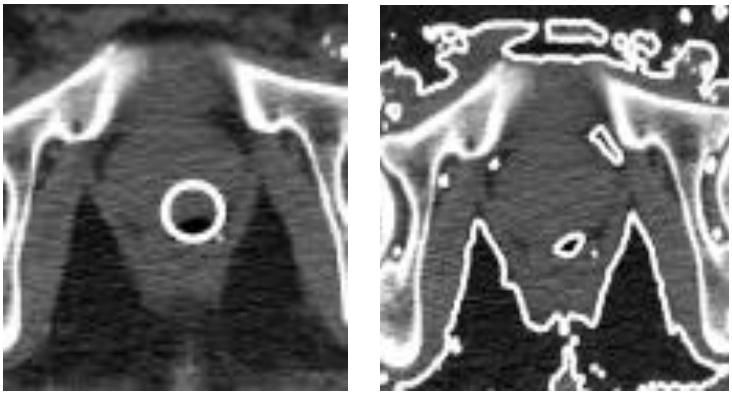

Figure 10. (Left panel) Initial segmenting contour. (Right panel) Outcome of the Chan and Vese segmentation algorithm using the piece-wise constant Mumford-Shah model.

Figures 11, 13, 15 and 17 show the segmentation outcomes in 2D and 3D (white contour) on CT and MRI images respectively. The gray contour on the same image depicts the manual segmentation performed by a physician/medical physicist. The 3D structure created by stacking all the 2D segmenting contours is shown in figures 12 and 16. The final 3D segmenting surface generated by the GA for 3D segmentation is shown in figures 14 and 18. Note that 2D segmentations do not use pixel and contour location information across slices, therefore the final segmenting curves are not well aligned with respect to each other when stacked to create a 3D object. In contrast, the 3D segmenting curves are well-aligned across slices of the same scan, because they incorporate information of the shape of the segmenting curve and pixel variations from different slices. Figure 19 shows the plot of average fitness of the population as a function of the number of generations of the GA obtained from the 3D segmentation of a CT image. The figure shows that the fitness of the GA population increased with time depicting that better segmentation outcomes were found by the GA with each generation. Since this fitness function is based only on the average value of the texture parameter inside and outside the segmenting contour, a perfect (1000) or a nearly perfect fitness score can only be obtained if there are prominent textural differences between the segmented region and outside. This is not the case for pelvic images, because the prostate is not very texturally distinct from its neighboring organs. This is evident from the 2D segmentation results where the GA was only able to converge to the approximate prostate region using the relative location map for 2D segmentation. The segmentation outcomes in 3D were better than 2D because textural and position information across slices aided better localization of the prostate by the GA on the pelvic images.

The visual evaluation of the segmentations by medical experts (A.H. and J.T.) was identified as satisfactory for locating the prostate on the pelvic CT/MRI images. The evaluation of the exact boundary segmenting contours was performed by computing the average dice similarity coefficient value obtained from the 2D/3D segmentations as shown in Table 2. Inaccuracies in the segmentation as reflected by the DSC values can be accounted by the fact that the shape model was computed from a training set of only 5 patients, which is too small to create a generalized model of the "average" shape variations over all patients. In future, the methodology could be extended to generate patient-specific models using multiple scans of the same patient, so that automated segmentations can be performed on new scans using information derived from manual segmentations on prior scans of the same patient.

Table 2 *DSC* values showing segmentation overlap with the ground truth

| | |
|---|---|
| 2D Segmentation | 0.45 |
| 3D Segmentation | 0.69 |

.

Using a genetic algorithm instead of a conventional gradient descent optimization offered the following advantages:

1. Flexibility: The genetic algorithm optimized an implicit fitness function instead of an explicit energy function term. This made it flexible to incorporate multiple features for performing segmentation without modifying the fitness function.

2. Generalizability: Genetic algorithms, like other evolutionary optimization techniques, have more generalizability than traditional optimization methods. The method could be extended to a larger set of features to solve other segmentation problems.

A genetic algorithm also has the following limitations:

1. Computational complexity: The computational time of the GA is a linear function of the population size ($S$) and the number of generations ($G$) and is given by $O(S \cdot G)$. Parallel implementation [57] with GPUs could be used to significantly speed up the computation time and is a subject of future work.

2. Precision: Although the outcomes of a genetic algorithm on repeated trials are close, they are not identical. However, given the subjectivity in the definition of tumor margins for pelvic CT/MRI images, deriving an approximate outline of tumor boundaries can significantly speed up the treatment planning process.

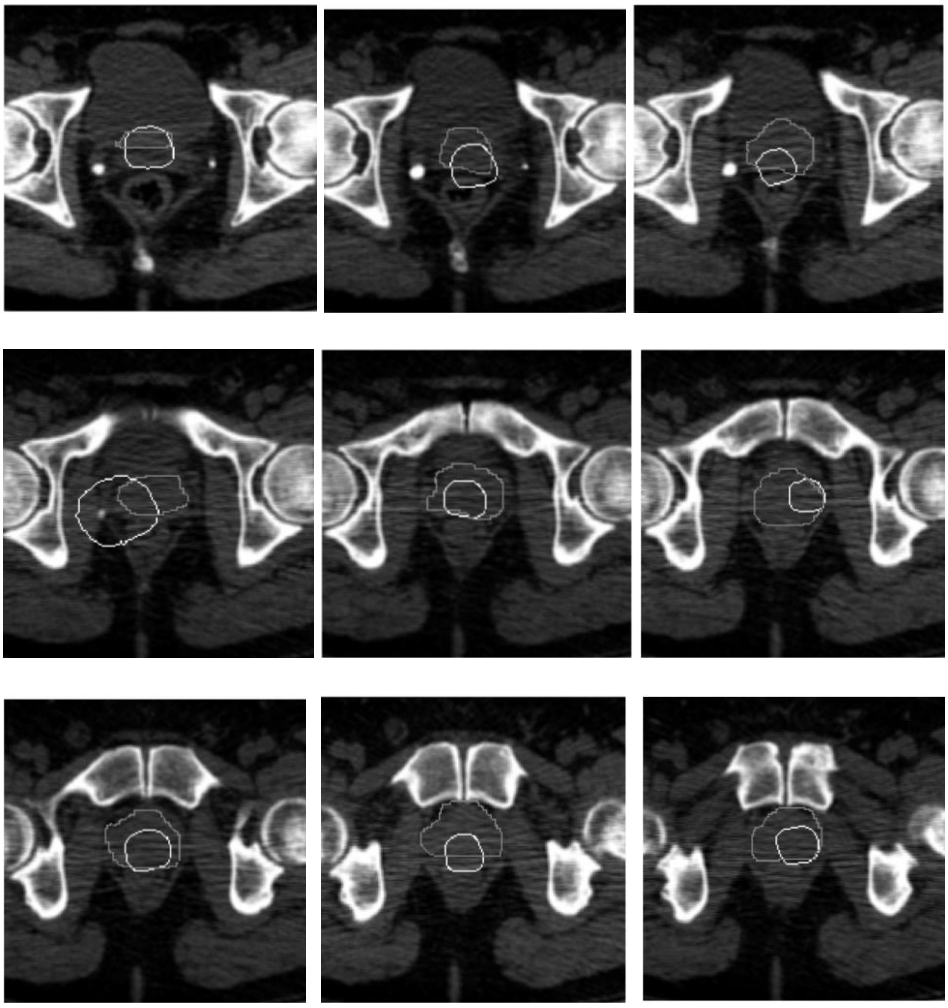

Figure 11. 2D segmentation results on a CT image using the GA.

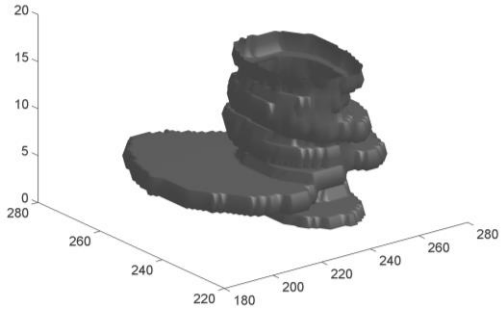


Figure 12. Segmenting contours of 2D segmentation stacked to form a 3D shape.

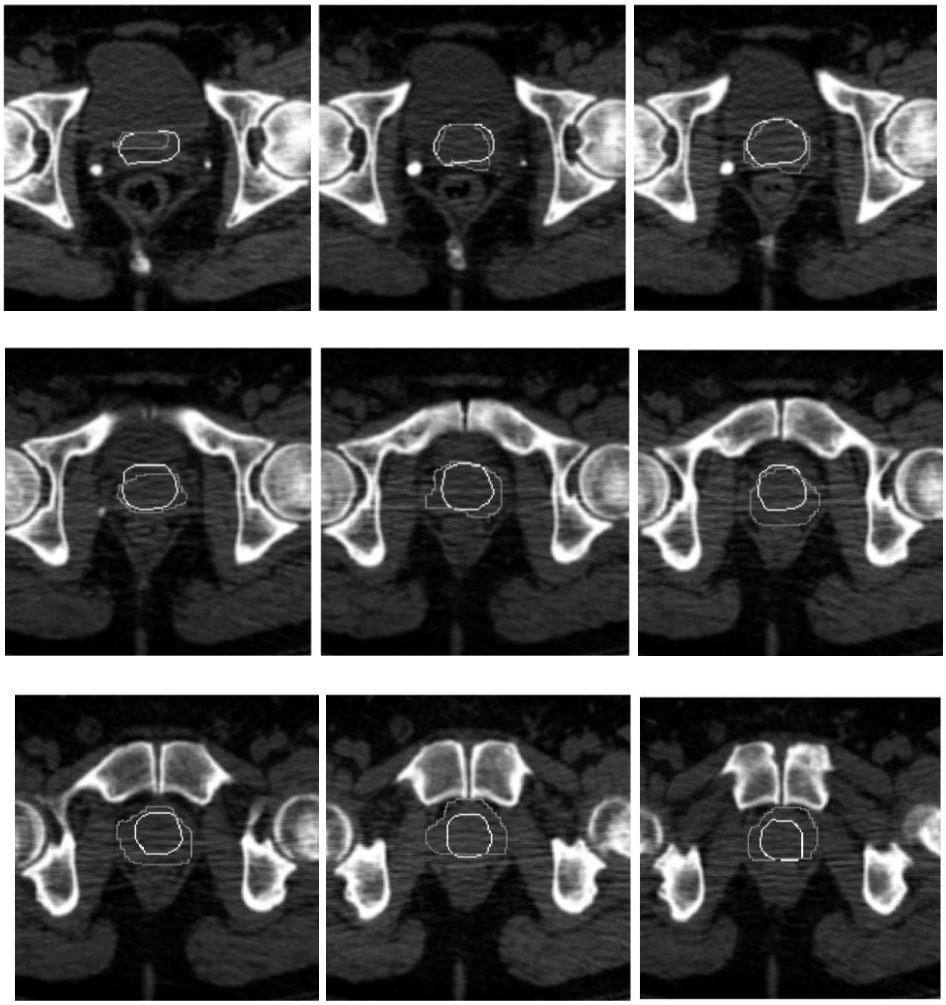

Figure 13. 3D segmentation of a CT image using the GA.

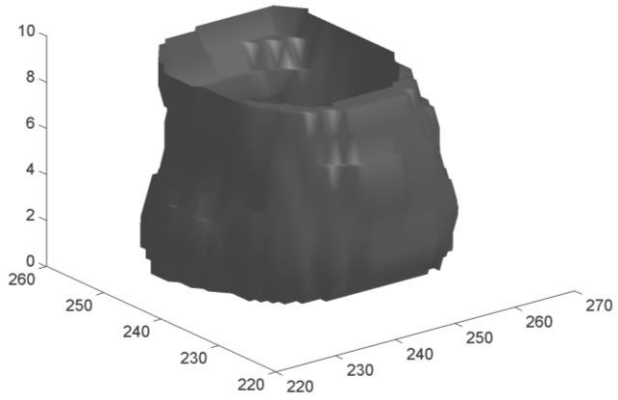


Figure 14. 3D segmenting surface generated by the GA.

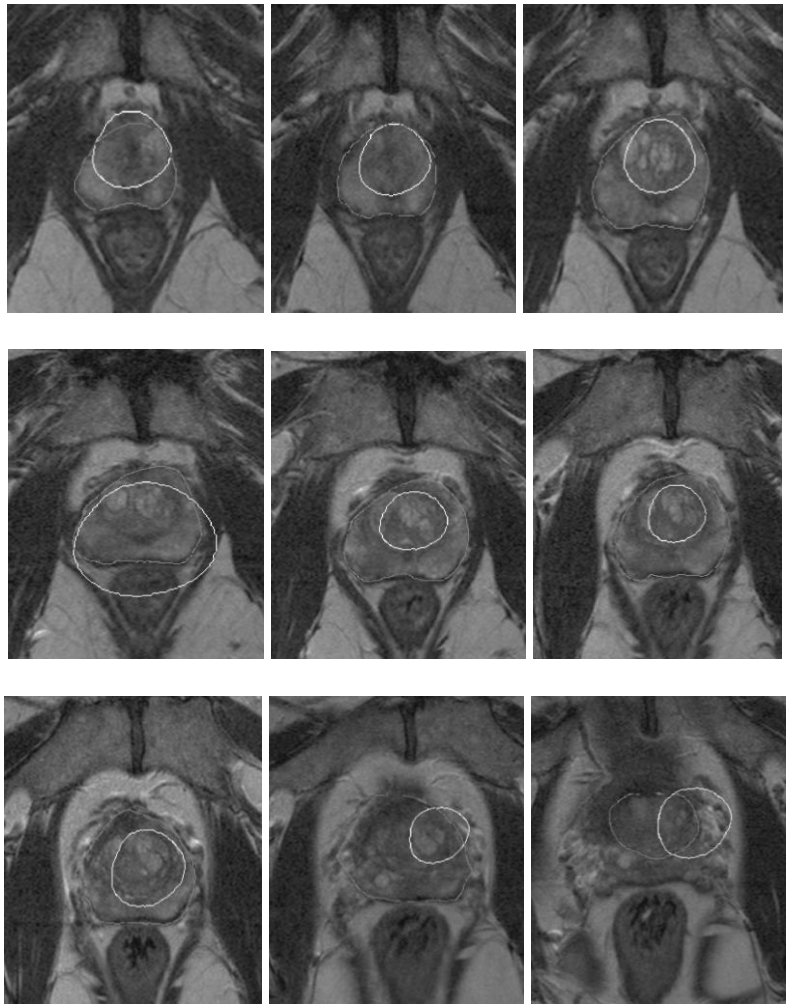

Figure 15. 2D segmentation of an MRI image using the GA.

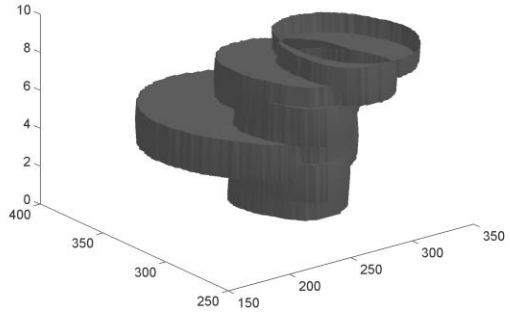


Figure 16. 2D Segmenting contours stacked together to form a 3D shape.

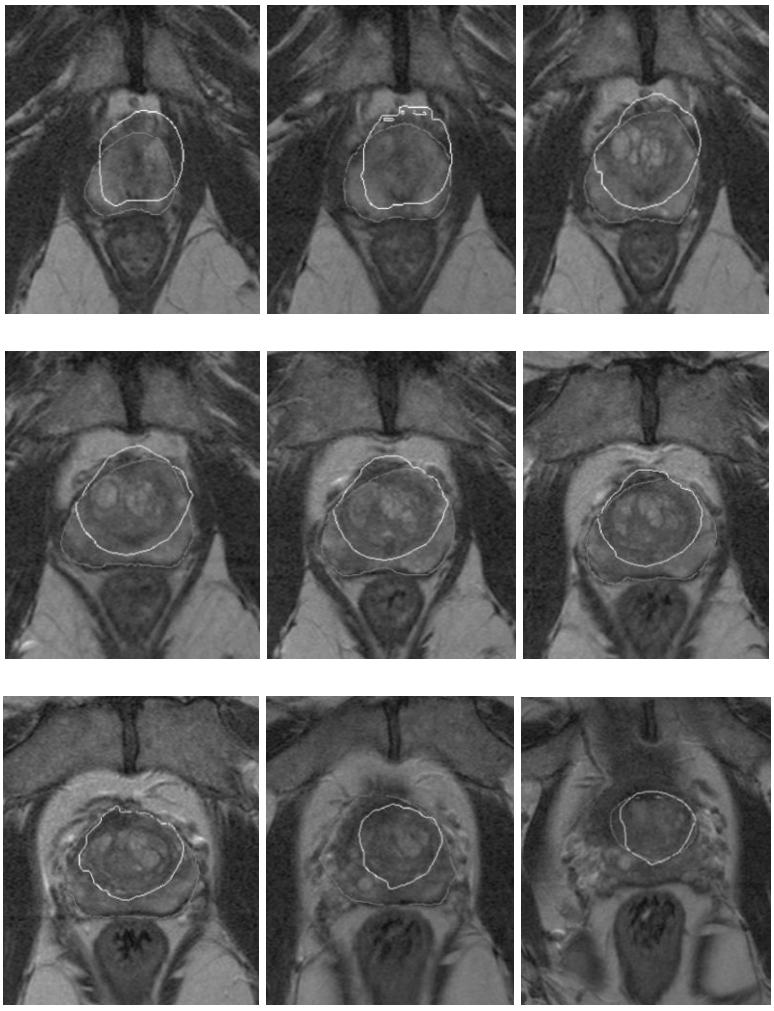

Figure 17. 3D segmentation of an MRI image using the GA.

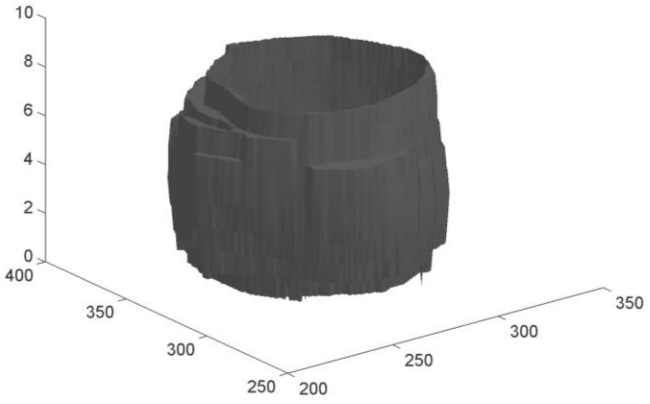


Figure 18. Segmenting surface generated by the GA.

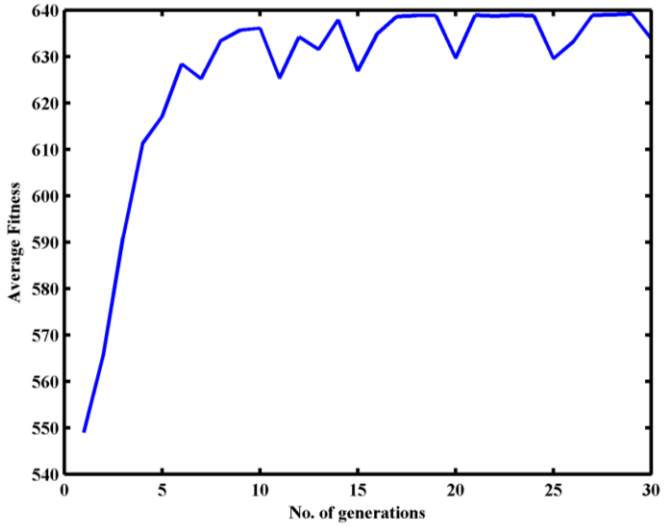


Figure 19. Plot of average fitness versus the number of generations for 3D segmentation of a CT image.

## VII. Conclusion

The GA presented here performs derivative-free optimization of a level set function for image segmentation. Representing candidate solutions of the GA as segmenting contours and assessing their performance using a fitness function eliminates the need for defining an energy function and simplifies the optimization procedure needed for image segmentation. This enables the incorporation of different kinds of priors for exploring the fitness landscape. The visual analysis of the results confirms that the GA performs satisfactory segmentation of the pelvic CT and MRI images. Performing segmentation in three dimensions improves the alignment of the segmenting contours across slices. Incorporating spatial relationships into the GA narrows the search space of the GA to the region between the bladder and the rectum. The methodology could be extended in future to develop patient specific models to speed up radiation therapy treatment planning.

## Acknowledgements

This research was partially funded by Intel Corporation and the J. S. McDonnell Foundation. The authors would also like to thank Dr. Xubo Song and Kun Yang for valuable discussions on this project.

## References


[1] P. Ghosh, M. Mitchell, J. Gold, "LSGA: Combining level-sets and genetic algorithms for segmentation," *Evolutionary Intelligence*, vol. 3, pp. 1-11, 2010.

[2] L. He, Z. Peng, B. Everding, X. Wang, C. Y. Han, K. L. Weiss, & W. G. Wee, "A comparative study of deformable contour methods on medical image segmentation," *Image and Vision Computing*, vol. 26(2), pp. 141-163. 2008.

[3] A. Mahr, S. Levegrun, M. L. Bahner, J. Kress, I. Zuna, & W. Schlegel, "Usability of semiautomatic segmentation algorithms for tumor volume determination," *Invest. Radiolog*., vol. 34, pp.143-150, 1999.

[4] T. McInerney, D. Terzopoulos, "Deformable models in medical image analysis: A survey," *Medical image analysis*, 1(2), 91-108, 1996.

[5] J. H. Holland, *Adaptation in Natural and Artificial Systems*. Ann Arbor, MI, University of Michigan Press, 1975.

[6] M. Mitchell, *An introduction to genetic algorithms*. Cambridge, MA: MIT Press, 1996.

[7] D. E. Goldberg. *Genetic Algorithms in Search, Optimization and Machine Learning*. Reading, MA: 1st Addison-Wesley Longman Publishing Co Inc, 1989.

[8] C. Harris, B. Buxton, "Evolving edge detectors," Research Note RN/96/3, University College, Dept. of Computer Science, London, 1996.

[9] N. Harvey, R. M. Levenson, D. L. Rimm, "Investigation of automated feature extraction techniques for applications in cancer detection from multi-spectral histopathology images," *Proc of SPIE*, 5032, 557-566, 2003.

[10] P. Nordin, W. Banzhaf, "Programmatic compression of images and sound," in Koza, J. R. et al. (Eds.), *Proceedings of the 1st Annual Conference on Genetic Programming*. Morgan Kaufmann, San Francisco, CA, 1996.

[11] N. Harvey, et al. "Comparison of GENIE and conventional supervised classifiers for multispectral image feature extraction," IEEE Transactions on Geoscience and Remote Sensing, 40(2), 393-404, 2002.

[12] J. A. Sethian, *Level set methods and fast marching methods*. New York, NY: Cambridge University Press, 1999.

[13] S. J. Osher, R. P. Fedkiw, *Level set methods and dynamic implicit surfaces*. New York, NY: Springer, 2002.

[14] A. Ahmadian, A. Mostafa, "An efficient texture classification algorithm using Gabor wavelet," In *Proceedings of the 25th Annual International Conference of the IEEE EMBS*, 930-933, Washington, DC: IEEE press, 2003.

[15] T. Chan, L. Vese, "Active contours without edges," *IEEE Trans. on Image Proc.*, 10, 266-277, 2001.

[16] R. Buxton. *Introduction of Functional Magnetic Resonance Imaging, Principles and Techniques*. Cambridge, UK: Cambridge University Press, 2003.

[17] M. Tuseryan, "Model based texture segmentation," *Pattern Recognition Letters*, 15, 659-668, 2004.

[18] M. Sonka, V. Hlavac, R. Boyle. *Image processing, analysis and machine vision*. London, UK: Chapman & Hall, 1994.

[19] J. J. Kulikowski, S. Marcelja, P. Bishop, "Theory of spatial position and spatial frequency relations in the receptive fields of simple cells in the visual cortex," *Biol. Cybern*, 43,187-198, 1982.

[20] J. Shi, J. Malik, "Normalized cuts and image segmentation," *IEEE Transactions on Pattern Analysis and Machine Intelligence*, 22(8), 888-905, 2000.

[21] J. M. Coggins, A.K. Jain, "A spatial filtering approach to texture analysis," Pattern Recognition Letters, 3, 195–203, 1985.

[22] D. Dunn, W.E. Higgins, "Optimal Gabor filters for texture segmentation," *IEEE Transactions on Image Processing*, 4(7), 947-964, 1995.

[23] K. I. Laws, "Texture Image Segmentation," Ph.D. dissertation, Univ. of Southern California, 1980.

[24] G. C. Cross, A. K. Jain, "Markov random field texture models," *IEEE Transactions on Pattern Analysis and Machine Intelligence*, 5, 25–39, 1983.

[25] R. L. Kashyap, R. Chellappa, N. Ahuja, "Decision rules for the choice of neighbors in random field models of images," *Computer Graphics and Image Processing*, 15, 301–318, 1981.

[26] A. P. Pentland, "Fractal-based description of natural scenes," *IEEE Transactions on Pattern Analysis and Machine Intelligence*, 6(6), 661–674, 1984.

[27] S. J. Osher, R. P. Fedkiw, "Level set methods and dynamic implicit surfaces," New York, NY: Springer, 2002.

[28] R. Malladi, J. A. Sethian, B. C. Vemuri, "Shape modeling with front propagation: A level set approach," *IEEE Trans on Patt Anal and Machine Intell*, 17(2), 158-175, 1995.

[29] J. A. Sethian, *Level set methods and fast marching methods*. New York, NY: Cambridge University Press, 1999.

[30] D. Cremers, M. Rousson, R. Deriche, "A review of statistical approaches to level set segmentation: Integrating color, texture, motion and shape," *Intl. J. of Comp. Vis.*, 72(2), 195-215, 2007.

[31] M. Leventon, E. Grimson, O. Faugeras, "Statistical shape influence in geodesic active contours," in *Proc. of IEEE Conference on Computer Vision and Pattern Recognition*, 1, 316-323, IEEE Press, 2000.

[32] A. Tsai, A. Yezzi, W. Wells, C. Tempany, D. Tucker, A. Fan, E. Grimson, , A. Willsky, "A shape-based approach to the segmentation of medical imagery using level sets," *IEEE Transactions on Medical Imaging*, 22, 137-154, 2003.

[33] P. Etyngier, F. Segonne, R. Keriven, "Active contour-based image segmentation using machine learning techniques," in *Proceedings of the Medical Image Computing and Computer-Assisted Intervention Conference*, 891-900, Heidelberg, Germany: Springer.

[34] T. Chan, L. Vese, "Active contours without edges," *IEEE Trans. on Image Proc.*, 10, 266-277, 2001.

[35] I. Bloch, "Fuzzy methods in medical imaging," in N. Ayache, J. Duncan and N. Paragios (Eds.), *The Handbook of Biomedical Image Analysis*. Heidelberg, Germany: Springer, 2009.

[36] D. M. Mark, M. J. Egenhofer, "Modeling spatial relations between lines and regions: combining formal mathematical models and human subjects testing," *Cartography and Geographic Information Systems*, October 1994, 21(4), 195-212.

[37] M. Yang, Y. Wu, G. Hua, "Context-aware visual tracking," IEEE Trans. on Pattern Anal. and Mach. Intell., 31(7), 1195-1209, 2009.

[38] L. Vieu, "Spatial representation and reasoning in artificial intelligence," in Stock, O. (Ed.), *Spatial and Temporal Reasoning*, 5-41. Alphen aan den Rijn, Netherlands: Kluwer, 1997.

[39] M. Skubic, S. Blisard, C. Bailey, J. Adams, P. Matsakis, "Qualitative analysis of sketched route maps: translating a sketch into linguistic descriptions," *IEEE Trans. Syst. Man, Cybern.- Part B: Cybern*, 34(2), 1275-1282, 2004.

[40] T. V. Pham, A. W. M. Smeulders, "Learning spatial relationships in object recognition," *Pattern Recognition Letters*, 27, 1673-1684, 2006.

[41] K. Miyajima, A. Ralescu, " Spatial organization in 2D segmented images: Representation and recognition of primitive spatial relations," Fuzzy Sets and Systems, 65(2/3), 225-236, 1994.

[42] H. Bunke, "Graph matching for visual object recognition," *Spatial Vision*, 13, 335–340, 2000.

[43] I. Bloch, "Fuzzy relative location between objects in image processing: a morphological approach," *IEEE trans. on Patt. Ana. Mach. Intell*., 21(7), 657-664, 1999.

[44] I. Bloch, "Fuzzy methods in medical imaging," in N. Ayache, J. Duncan and N. Paragios (Eds.), The *Handbook of Biomedical Image Analysis*. Heidelberg, Germany: Springer, 2009.

[45] R. Poli, S. Cagoni, "Genetic programming with user-driven selection: Experiments on the evolution of algorithms for image enhancement," in *Proceedings of the 2nd Annual Conference on Genetic Programming* (pp. 269-277). San Francisco, CA: Morgan Kaufmann, 1997.

[46] J. M. Daida, J. D. Hommes, T. F. Bersano-Begey, S. J. Ross, J. F. Vesecky, "Algorithm discovery using the genetic programming paradigm: Extracting low-contrast curvilinear features from SAR images of Arctic ice," in P. J. Angeline & K. E. Kinnear Jr. (Eds.), *Advances in Genetic Programming 2*, 417-442. Cambridge, MA: MIT press, 1996.

[47] Y. M. B., Ali, "Edge-based segmentation using robust evolutionary algorithm applied to medical images," *Journal of Signal Processing Systems*, 54(1), 231 – 238, 2009.

[48] R.A. Caruana, J. D. Schaffer, "Representation and Hidden Bias: Gray vs. Binary Coding. Proc. 6th Int. Conf. Machine Learning," 153-161, 1988.

[49] B. Bhanu, S. Lee, J. Ming, "Adaptive image segmentation using a genetic algorithm," *IEEE Transactions on Systems Man and Cybernetics*, 25(12), 1543-1567, 1995.

[50] L. Ballerini, "Genetic Snakes for Medical Images Segmentation," in Poli, R. et al. (Eds.), *Proceedings of the First European Workshops on Evolutionary Image Analysis, Signal Processing and Telecommunications*, *Lecture Notes In Computer Science*, 1596, 59-73, London, UK: Springer-Verlag, 1999.

[51] A. Cagnoni, A. B. Dobrzeniecki, R. Poli, J. C. Yanch, "Genetic algorithm-based interactive segmentation of 3D medical images," *Image and Vision Computing*, 17(12), 881-895, 1999.

[52] J. Dehmeshki, X. Ye, X. Lin, M. Valdivieso, H. Amin, "Automated detection of lung nodules in CT images using shape-based genetic algorithm," *Computerized Medical Imaging and Graphics*, 31(6), 408-417, 2007.

[53] S. Chabrier, C. Rosenburger, B. Emile, B., H. Laurent, "Optimization based image segmentation by genetic algorithms," *EURASIP Journal on Video and Image Processing*, 1-23, 2008.

[54] M. Kass, A. Witkin, D. Terzopoulos, D., "Snakes: Active contour models," *International Journal of Computer Vision*, 1, 321-331, 1988.

[55] J. Louchet, "Model-based image analysis using evolutionary computation," in *Genetic and Evolutionary Computation for Image processing and Analysis*, New York, NY: Hindawi, 2007.

[56] Dice, L.R., "Measures of the amount of ecologic association between species," *Ecology*, 26:297-302, 1945.

[57] Luque, G., Alba, E., & Dorronsoro, B. (2005). Parallel genetic algorithms. In E. Alba (Ed.), Parallel metaheuristics: A new class of algorithms, 107-126. Hoboken, NJ: John Wiley & Sons Inc.